merely a device that oscillates, a "clock" represents "[a]ny instrument for measuring or indicating time" and a "pacemaker" is defined as a process or substance that "regulates" the timing of other events (*19*). Although the capacity to oscillate is a widely distributed property, the restoration of circadian rhythmicity in SCN-lesioned, arrhythmic hosts by immortalized SCN cells but not NIH 3T3 mouse fibroblasts implies that only oscillators derived from the SCN act as pacemakers and have the capability to impose their rhythmicity on mammalian behavior. How these oscillators in the SCN drive rhythms in behavior is unclear at this point, but there is increasing evidence indicating that the SCN secretes a diffusible factor that at least in part contributes to this rhythmic efflux (*20*). Perhaps one of these factors is a neurotrophin such as BDNF or NT-3, based on their rhythmic expression in immortalized SCN cells and the SCN in vivo (*14*).

References and Notes

1. U. Albrecht, Z. S. Sun, G. Eichele, C. C. Lee, *Cell* **91**, 1055 (1997).
2. L. P. Shearman, M. J. Zylka, D. R. Weaver, L. F. Kolakowski, S. M. Reppert, *Neuron* **19**, 1261 (1997).
3. Y. Shigeyoshi *et al.*, *Cell* **91**, 1043 (1997).
4. Z. S. Sun *et al.*, *ibid.* **90**, 1003 (1997).
5. H. Tei *et al.*, *Nature* **389**, 512 (1998).
6. M. J. Zylka, L. P. Shearman, D. R. Weaver, S. M. Reppert, *Neuron* **20**, 1103 (1998).
7. A. Balsalobre, F. Damiola, U. Schibler, *Cell* **93**, 929 (1998).
8. D. J. Earnest *et al.*, *J. Neurobiol.*, in press.
9. W. J. Schwartz, in *Suprachiasmatic Nucleus: The Mind's Clock*, D. C. Klein, R. Y. Moore, S. M. Reppert, Eds. (Oxford Univ. Press, New York, 1991), pp. 144–156.
10. G. C. Newman and F. E. Hospod, *Brain Res.* **381**, 345 (1986).
11. The SCN2.2 cell line is derived from fetal progenitors of the rat SCN (embryonic day 15) immortalized with the adenovirus E1A gene (*8*). Cells derived from a single passage were expanded onto multiple dishes (60 mm) coated with mouse laminin and maintained in minimum essential medium containing 10% fetal bovine serum, glucose (2 μg/ml), and L-glutamine (292 μg/ml) under constant temperature (37°C) and 5% CO_2. At 4-hour intervals for 2 days, confluent cultures (N = 5) were incubated for 1 hour with ^{14}C-labeled 2-DG (0.2 mCi/ml; American Radiological Company, St. Louis, MO). Fractional products of 2-DG metabolism were measured with the methods described by Newman and colleagues [G. C. Newman, F. E. Hospod, C. S. Patlak, *J. Cereb. Blood Flow Metab.* **10**, 510 (1990)]. Fractions derived from 2-DG, 2-DG-6P, free 2-DG, and glycogen compartments were placed in scintillation vials in triplicate, dried before addition of scintillant, and then counted on a Beckman scintillation counter.
12. Portions (25 μl) of recovered protein from these samples were also assayed in triplicate for BDNF and NT-3 content by enzyme-linked immunosorbent assay (*2*). The intra-assay and interassay coefficients of variation were less than 5 and 10%, respectively. BDNF and NT-3 levels were quantified within the linear range of their standard curves (1 to 250 ng/ml and 4.7 to 300 pg/ml, respectively). The antibodies to BDNF and NT-3 in these assays show less than 2% cross reactivity with structurally similar neurotrophins (at 10 μg/ml). Determinations of ^{14}C-labeled 2-DG uptake and neurotrophin content were normalized for sample protein content as measured by the bicinchoninic acid method (Pierce). This analysis was replicated on three separate sets of cultures. Time-dependent alterations in glucose utilization and neurotrophin levels were identified with one-way analysis of variance, and differences between determinations at distinct time points were tested post hoc for significance with the Newman-Keuls sequential range test.
13. F.-Q. Liang, F. Sohrabji, R. Miranda, B. Earnest, D. Earnest, *Exp. Neurol.* **151**, 184 (1998).
14. F.-Q. Liang, R. Walline, D. J. Earnest, *Neurosci. Lett.* **242**, 89 (1998).
15. Male adult Sprague-Dawley rats (150 to 200 g) were housed in individual cages, and wheel-running activity was continuously recorded with Dataquest IV software (Data Sciences, St. Paul, MN). Animals were exposed to a standard 12 hour light:12 hour dark photoperiod (LD) for 7 to 10 days and then maintained under dim constant light (LL; 5 to 10 lux). After 2 to 4 weeks of baseline recording, animals were anesthetized (Xylazine, 2 mg/kg; Ketamine, 10 mg/kg), and with the use of stereotaxic coordinates, SCN lesions were generated by current injection (4 mA for 15 s) through a Teflon-coated tungsten wire (0.203 mm). Animals exhibiting a loss of circadian rhythmicity in their activity behavior for 6 to 8 weeks received transplants of either SCN2.2 cells, E1A-immortalized mesencephalic progenitors, or NIH 3T3 fibroblasts. Colonies of these cell lines were harvested by enzymatic (0.125% trypsin) disaggregation and immediately transplanted as aggregates of 200,000 cells in Hanks' balanced salt solution into the periventricular third ventricle region of anesthetized recipients. Some cultures were preincubated with the carbocyanine dye DiI (12 μg/ml) to allow selective identification of transplanted cells in host brain sections by fluorescence microscopy. Activity records during SCN intact, postlesion, and posttransplantation intervals were separately analyzed for evidence of circadian rhythmicity with χ^2 periodogram (Tau) and fast Fourier transform analyses. After behavioral analysis, animals were killed with sodium pentobarbital (3.0 mg/kg) and perfused transcardially with 4% paraformaldehyde in 0.1 M phosphate buffer. Animal care and procedures were performed in compliance with state law, federal statute, and NIH policy.
16. Brains were prepared for histological processing as described previously (*13*). Coronal sections (30 μm) were separately processed for immunocytochemical analysis with antibodies to GRP, VIP (1:1500 and 1:5000, respectively; Peninsula Laboratories, Belmont, CA), AVP (1:10,000; Arnel Labs, New York), or BDNF (1:500; Promega, Madison, WI). No immunostaining for these antigens was observed within the host brain or grafts when the primary antisera was omitted or preincubated with homologous antigen (10^{-5} M), except for occasional light staining in the area of gliosis surrounding the lesion site.
17. R. Y. Moore, *Fed. Proc. Fed. Am. Soc. Exp. Biol.* **42**, 2783 (1983).
18. J. D. Plautz, M. Kaneko, J. C. Hall, S. A. Kay, *Science* **278**, 1632 (1997).
19. *American Heritage Dictionary of the English Language* (Houghton Mifflin, Boston, MA, 1979).
20. R. Silver, J. LeSauter, P. A. Tresco, M. Lehman, *Nature* **382**, 810 (1996).

21. We thank D. Bell-Pedersen for comments on the manuscript. This study was supported by NSF grant IBN-9511238 (D.J.E.) and NIH grant NS35822 (V.M.C.).

21 September 1998; accepted 22 December 1998

Horizontal Propagation of Visual Activity in the Synaptic Integration Field of Area 17 Neurons

Vincent Bringuier,* Frédéric Chavane, Larry Glaeser, Yves Frégnac†

The receptive field of a visual neuron is classically defined as the region of space (or retina) where a visual stimulus evokes a change in its firing activity. At the cortical level, a challenging issue concerns the roles of feedforward, local recurrent, intracortical, and cortico-cortical feedback connectivity in receptive field properties. Intracellular recordings in cat area 17 showed that the visually evoked synaptic integration field extends over a much larger area than that established on the basis of spike activity. Synaptic depolarizing responses to stimuli flashed at increasing distances from the center of the receptive field decreased in strength, whereas their onset latency increased. These findings suggest that subthreshold responses in the unresponsive region surrounding the classical discharge field result from the integration of visual activation waves spread by slowly conducting horizontal axons within primary visual cortex.

The average size of the minimal discharge field (MDF) in area 17 neurons is ~2° of visual angle (for the representation near the area centralis) when it is mapped with a small spot or slit of light (*1*, *2*). The strength of the spiking response results from the amplification of the feedforward thalamo-cortical drive by a local recurrent intracortical loop that preserves the retinotopic mapping of visual input onto cortex (*1*, *3*). However, firing responses to stimuli presented within the MDF can also be modulated by the concomitant stimulation of its surround, over a region up to 10° of relative eccentricity (*4*, *5*). These

Equipe Cognisciences, Institut Alfred Fessard, CNRS, Avenue de la Terrasse, 91198 Gif-sur-Yvette, France.

*Present address: Neurobiology Division, Medical Research Council LMB, 2 Hills Road, Cambridge CB22QH, UK.

†To whom correspondence should be addressed. E-mail: yves.fregnac@iaf.cnrs-gif.fr

center-surround interactions are thought to be mediated by long-range connections, which originate within area 17 (*6*), or from higher cortical areas (*7*). In vivo intracellular recording techniques allow the analysis of subthreshold synaptic inputs and their retinal origin (*8*, *9*). They were applied here to dissect out the different synaptic contributions potentially involved in binding information originating from distant parts of the visual field.

We performed intracellular sharp and patch recordings in the primary visual cortex of cat (*10*), using three mapping protocols, which evoked different degrees of spatial and temporal summation (*11*). First, brief punctate stimuli of positive or negative contrast were sequentially flashed in random positions in the visual field [two-dimensional (2D) impulse-like input]. Second, optimally oriented bars whose length matched that of the MDF length were flashed for longer duration in random positions across the receptive field width. Third, sinusoidal luminance gratings were presented through large co-centered annular windows, resulting in a high level of input summation. The stimulus-locked analysis of the membrane potential responses of 66 cells showed that visual cortical neurons were synaptically activated by stimuli well beyond the boundaries of their discharge field. Figure 1A illustrates a typical 2D impulse response field, with a compact MDF (2° by 1.6°), surrounded by a homogeneous subthreshold depolarizing field (D-field) (3.2° by 3.2°). Figure 1B illustrates, for another cell, the MDF (1.8°) and the subthreshold field (9°; D-field alone: 6.3°) when stimulating with long bars. Figure 1C illustrates the case of subthreshold depolarizing responses evoked by annular gratings even when separated from the MDF center by more than 11.3°.

Two parameters characterizing the spatial sensitivity profile of the synaptic integration field were extracted at the population level: mean spatial attenuation gradient and mean spatial extent of the subthreshold responses. Because in most cells at rest impulse-like input evoked mainly depolarizations, the strength of the significant depolarizing responses for the three mapping protocols is plotted in Fig. 2 as a function of the distance between the actual stimulus position and the location in the visual field eliciting the maximal spike discharge (*12*). The spatial sensitivity envelope of the D-field was generally co-centered with the MDF and declined with relative eccentricity. D-fields mapped with random 2D impulse-like inputs were characterized for each cell by a linear (mean correlation coefficient $\langle r \rangle = -0.83$), steep ($-24.3 \pm 15.9\%$ per degree) decrease of the postsynaptic response strength, at increasing distances from the MDF center (Fig. 2B). The same analysis for long bars gave a similar gradient estimate ($-23.7 \pm 16.7\%$ per degree; mean $\langle r \rangle = -0.82$, Fig. 2C). In contrast, the slope for gratings was significantly attenuated when compared with the 2D impulse-like input ($-16.8 \pm 13.4\%$ per degree in Fig. 2D; $P < 0.05$).

We estimated the boundary of the D-field by the angular distance between the extreme locations where the linear fits of each flank of the spatial sensitivity hill (measured along the MDF width or length axis, or both) intercepts the threshold level of significant response. The mean D-field outer diameter was 6.6 ± 4.3° ($n = 26$) for 2D impulse-like input, slightly less than that observed with long bars (8.5 ± 4.3°; $n = 20$). When gratings were used, because of the internal symmetry of the annular stimulus, only a lower bound estimate of the D-field boundary could be extracted (half width of the inner rectangle); this value was 14.6 ± 8.6° ($n = 19$). Thus, independently of its precise shape, the extent

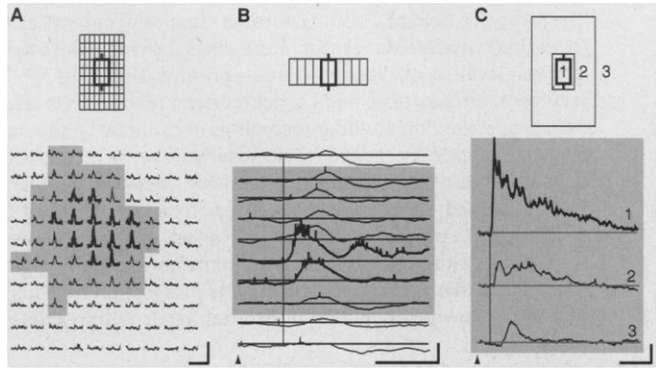

Fig. 1. Mapping the synaptic integration field. The different protocols (**A** to **C**) are symbolized in the upper row, with the preferred orientation of the recorded cell being set to vertical by convention. For each graph, synaptic responses eliciting spikes and defining the MDF extent are illustrated in bold. Shaded background delineates the region (or regions) where the significant subthreshold depolarizing responses are found. The stimulus onset is indicated by a black triangle in (B) and (C). Scale bars are 5 mV (vertical) and 100 ms (horizontal). (A) Two-dimensional impulse-like input: ON responses (averaged over 36 trials) to light patches (0.4° by 0.4°, 50 ms duration) in a unimodal simple cell. (B) Optimally oriented bars: averaged responses (15 trials) to dark bars (0.9° by 3.9°, 1 s duration) in a complex cell in 10 contiguous positions. (C) Sinusoidal gratings: averaged ON responses (30 trials) to a stationary optimally oriented grating in a simple cell. The grating is counterphased at 2 Hz in the MDF (region 1), or regions co-centered around it (2: NEAR periphery, 3: FAR periphery). Cells (A) and (B) were recorded in adult cats, and cell (C) in a 15-week-old kitten. Resting potential [dotted line in (B) and (C)] was −51 mV (A), −65 mV (B), and −62 mV (C). Retinal eccentricities of the discharge field centers were 1.3° (A), 3.9° (B), and 5.7° (C).

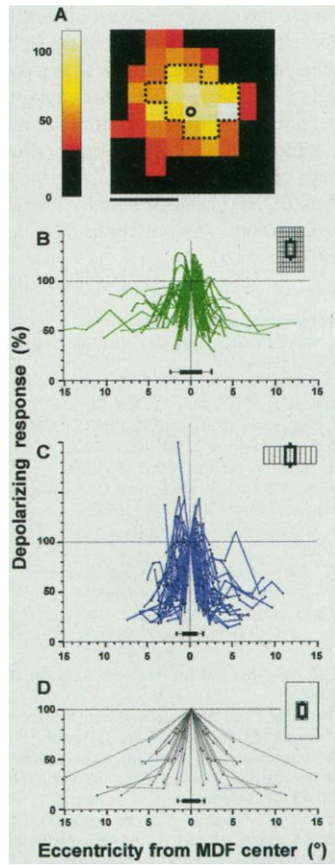

Fig. 2. Spatial profile of the depolarizing field. The visually evoked strength of the depolarizing response is normalized relative to that observed at the location of the MDF (dotted contour) eliciting the maximal discharge (circle). (**A**). Color-coded map of the response strength, obtained for the cell shown in Figs. 1A, 3A, and 4A. Black pixels indicate the absence of significant responses. Horizontal scale bar, 2°. (**B** to **D**) Each individual profile represents for a given cell the change in response strength across the width or length of the RF, expressed as a function of the eccentricity of the stimulus from the MDF center. These different profiles have been superimposed together on the same graph, each corresponding to a particular mapping protocol [(B) 2D impulse-like input ($n = 37$); (C) flashed bars ($n = 21$); (D) flashed ($n = 19$) or moving ($n = 2$) sinusoidal luminance gratings]. The average MDF extent and its SD are indicated by thick and thin horizontal line segments, respectively. In the case of annular stimuli, the abscissa corresponds to the distance between the center of the MDF and the inner radius of the annulus.

of the D-field increased beyond that of the MDF (2.74 ± 2.3° for impulse-like input and 2.5 ± 1.9° for long bars) by a factor dependent on the mapping stimulus (×2.5 for impulse-like input, ×3.3 for long bars, ×5.6 for gratings). These results show the existence of a large field of depolarizing responses whose detection is favored by spatiotemporal synaptic summation. This conclusion differs from the classical suppressive role attributed to surrounding regions of the cortical discharge field (*5*, *13*). It may also explain the additional excitatory drive provided by surrounding regions for bipartite center and surround stimulus configurations (*14*).

To measure quantitatively the topographic arrangement of the responsive areas, while distinguishing between spikes, excitatory, and inhibitory events (*15*), we devised a method adapted from the reverse correlation (RC) technique (*16*). This method allows us to assess which pixels in the visual field elicited a significant response at a preset confidence level (99%) (*17*). The occurrence times of several types of voltage events were detected in the filtered membrane potential signal, and each of the corresponding time-series was correlated with the random stimulus sequence. Three different receptive field maps were established for each neuron, based on the detection of spikes (MDF), of subthreshold depolarizing events (D-fields), and of hyperpolarizing events (H-fields) (Fig. 3). This analysis estimated the mean equivalent diameter of MDFs as 3.3 ± 1.3° and that of the D-field as 4.4 ± 2.4° (by compacting all responsive domains into a single disk of the same total area). In 30% of cases, the internal structure of the D-field was patchy, with one to four additional islands of subthreshold depolarizing responses, detached from the one co-centered with the MDF (Fig. 3C). Patchiness was even more apparent in the H-fields whose extent was more limited (equivalent diameter: 2 ± 1°). Thus, the topological union of the MDF, D-field, and H-field, that is, the synaptic integration field, on average covered an area (equivalent diameter: 5 ± 2.4°) that was four times as large as that of the MDF. This result, obtained when the cell is at rest, can only give a lower bound estimate of the maximal extent of recruitable synaptic input, the functional activation of which also depends on the voltage at which the cell is held.

A second source of information that could help to trace the origin of subthreshold responses is their onset latency (*18*). A strong correlation was observed in most cells between the latencies of the depolarizing response and the eccentricity of the flashed stimulus relative to the center of the MDF, giving an isotropic latency basin shape. The center of this basin corresponding to the shortest latencies was typically near the region of maximum discharge (*19*). We explored the hypothesis that the peripheral subthreshold depolarizing responses are relayed by horizontal connections within area 17 (*6*, *20*). According to this framework, the linear relation observed between the latency of the postsynaptic evoked depolarization and the stimulus eccentricity relative to the MDF center results from a constant propagation velocity of action potentials along intracortical axons. To test this prediction, we converted the distance separating two loci of activation in the visual field into a distance in the cortex. We used an average cortical magnification factor of 1 mm in the cortex for 1° in retinal space (*21*). The apparent speed of

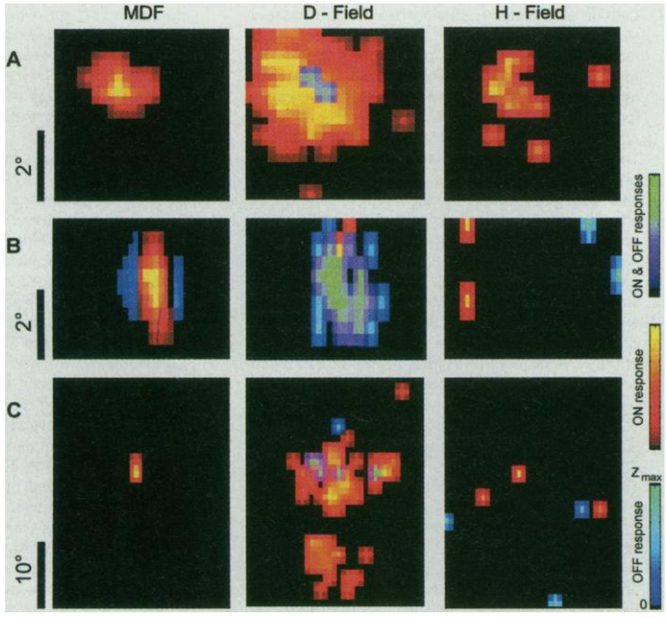

Fig. 3. Reverse correlation maps of the synaptic integration field. All color-coded maps (red: ON; blue: OFF) show, for all statistically significant pixels ($P < 0.01$), the *z* score of the optimized reverse correlation count (*17*). The zones of overlap between ON and OFF responses are illustrated by generating a transparency color map mixing linearly ON and OFF color codes. Black pixels indicate the absence of significant responses. The three columns illustrate the MDF (left), the D-Field (center), and the H-field (right) for three different cells recorded in adult cortex. The z_{max} scores (MDF, D-Field, H-Field) are, respectively, 17.5, 14, and 6.5 (A); 32, 6.5, and 3.5 (B); and 10, 8.5, and 4 (C). (**A**) The same cell as in Figs. 1A, 2A, and 4A, for which the RC method reveals a much larger integration field than stimulus-locked averaging. (**B**) Three-zone simple cell (OFF-ON-OFF). (**C**) Unimodal ON simple cell. Resting potential was −51 mV (A), −55 mV (B), and −59 mV (C). The stimulus sizes were 0.4° by 0.4° (A), 1.6° by 0.6° (B), and 1.89° by 1.39° (C). Retinal eccentricities of the discharge field centers were 1.3° (A), 5.1° (B), and 3.4° (C).

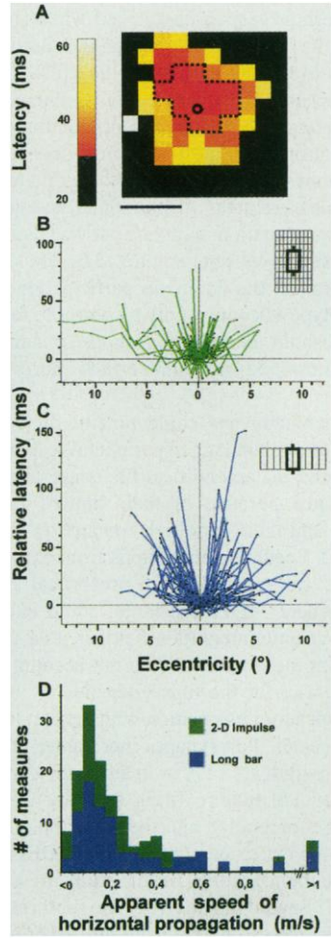

Fig. 4. Basin of latencies of subthreshold depolarizing synaptic responses. (**A**) Color-coded map of the absolute latency of the depolarizing response, obtained for the same cell and protocol as in Figs. 1A, 2A, and 3A. Black pixels indicate the absence of significant change in the onset slope of the postsynaptic response. In (**B**) and (**C**), the graphs represent changes in latency measured across the width or length of the RF and expressed as a function of the eccentricity of the stimulus from the latency basin center (*18*), for two mapping protocols [(B) 2D-impulse-like input (n = 37); (C) flashed bars (n = 27)]. (**D**) Distributions of the ASHP values calculated from the slopes of the basins of latency illustrated in (B) (green) and (C) (blue).

horizontal propagation (ASHP) of the hypothetical cortical wave of activity (distance in the cortical projection map/difference in visual latencies of the synaptic responses) can be derived directly from the inverse of the slope estimates of the latency basins. Distributions of the ASHP values (Fig. 4D) for both 2D impulse-like stimuli and long-bar stimulations peak at 0.1 m/s and are indistinguishable (unpaired t test, $P > 0.55$). The cortical dynamics extrapolated here match the slow velocity of activation waves monitored in vivo with optical imaging techniques along the supragranular layer plane [0.1 to 0.25 m/s (*22*)]. Moreover, the intracellular subthreshold responses, evoked when stimulating the "silent" surround of the discharge field with annular gratings to the exclusion of the discharge field center and its immediate periphery, were selective to orientation (*23*), which strongly suggests a cortical origin. Our electrophysiological estimates also match in vitro measurements of horizontal action potential propagation in rat and cat visual cortex at physiological temperature (*24*). Thus, our data suggest the dominant participation of a single type of connectivity responsible for the subthreshold peripheral responses, namely, that subserved by intracortical horizontal axons.

Other pathways could potentially be invoked to explain lagged peripheral responses. Diverging thalamocortical fibers are unlikely candidates because of their limited lateral spread and their very high conduction velocity (*25*). Feedback projections from extrastriate cortical areas, or from precortical structures where MDFs are large, could explain large synaptic integration fields in area 17 (*7, 26*). But these pathways do not account in a simple way for the linear dependency of latency on stimulus position with respect to the MDF center. Polysynaptic horizontal propagation within area 17, or in subcortical structures, would require firing at every step of synaptic integration and therefore the unsubstantiated existence of very large MDFs (*27*).

The main findings of this study are threefold: (i) Spatial sensitivity at the subthreshold level decreases linearly from the center to the periphery of the discharge field. (ii) The extent of the synaptic integration fields of primary visual cortical neurons spans a much larger window of visual space than the MDF. (iii) The latency of depolarizing responses increases linearly from the MDF center toward its surround. Cortical spatiotemporal dynamics may be viewed in two complementary ways: A focal visual stimulus evokes in cortex a radial wave of activity that spreads in the plane of cortical layers at a constant velocity over a radius of more than 10 mm. This is in agreement with recent optical imaging of the cortical point spread function (*22, 28*). Reciprocally, functional integration realized by the cortical cell may be described by the summation of propagated inputs originating from distant intracortical sources in a spatiotemporal coordinate system centered on its minimal discharge field. A straightforward prediction of this model is that synaptic summation may be optimized by adjusting the relative latencies of activation evoked through the feedforward pathway and the peripheral intracortical connectivity. This could explain the boosting of cortical responses by bipartite stimuli composed by low-contrast center and high-contrast surround features (*14*). This also suggests that the processing of new visual information arising in the center of the classical discharge field could be highly influenced by contextual information that was present a few tens of milliseconds earlier in the periphery.

References and Notes

1. D. H. Hubel and T. N. Wiesel, *J. Physiol.* **160**, 106 (1962).
2. G. Orban, *Stud. Brain Funct.* **11**, 365 (1984).
3. R. J. Douglas *et al.*, *Science* **269**, 981 (1995); R. C. Reid and J.-M. Alonso, *Nature* **378**, 281 (1995).
4. P. O. Bishop *et al.*, *J. Physiol. (London)* **219**, 625 (1971); L. Maffei and A. Fiorentini, *Vision Res.* **16**, 1131 (1976); G. C. De Angelis *et al.*, *J. Neurophysiol.* **71**, 347 (1994).
5. C. Y. Li and W. Li, *Vision Res.* **34**, 2337 (1994).
6. C. D. Gilbert and T. N. Wiesel, *J. Neurosci.* **3**, 1116 (1983).
7. P. Salin and J. Bullier, *Physiol. Rev.* **75**, 107 (1995).
8. O. Creutzfeldt and M. Ito, *Exp. Brain Res.* **6**, 324 (1968); R. J. Douglas and K. Martin, *J. Physiol (London)* **440**, 735 (1991); L. J. Borg-Graham *et al.*, *Nature* **393**, 369 (1998).
9. X. Pei *et al.*, *J. Neurosci.* **14**, 7130 (1994).
10. Cells in the primary visual cortex of anesthetized (Althesin) and paralyzed kitten and adult cats were recorded intracellularly for periods ranging from 30 to 615 min. Three-millimeter artificial pupils were used. Sharp electrode recordings (46 cells) were performed in bridge mode with 50 to 90 megohm glass pipettes filled with 2 M potassium methyl sulfate. The average resting membrane potential was −65.8 mV (±8.7 mV), input resistance ranged between 10 and 70 megohm, and spike height ranged between 35 and 70 mV. Whole-cell recordings (20 cells) were done with 2 to 5 megohm glass patch electrode filled with 140 mM potassium-gluconate [L. J. Borg-Graham *et al.*, *Nature* **393**, 369 (1998)]. Data processing and visual stimulation protocols used in-house software (G. Sadoc, Acquis1 Biologic CNRS-ANVAR). Because the different measurements (the spatial extent of the synaptic integration field, ASHP) were found to be independent of age, data obtained from kittens older than 6 weeks of age and adult cats were pooled.
11. Mapping protocols: (i) Light and dark patches (0.2 to 3.8°, mean 1.1°) were sequentially flashed for 33 or 50 ms in 80 to 400 positions (contrast: 0.60, background luminance: 5 cd/m^2). (ii) Light or dark bars were randomly flashed ON and OFF for 500 ms or 1 s, at various eccentricities from the MDF (10 positions along the width axis, 20 trials). (iii) Medium-contrast gratings were adjusted for optimal spatial and temporal frequencies and presented either moving or counterphased through annular windows whose inner width and length were preset multiples of the dimensions of the MDF (120 and 360%). Each protocol sequence was repeated 10 to 50 times. Discharge field center locations varied between 1 and 16° of retinal eccentricity, but most receptive fields were located within 10° around the area centralis. Because no significant differences in our measurements were found between simple cells (62% of our sample) and complex cells (38%), both types of receptive fields were pooled.
12. Estimates of the ratio of D-field size over MDF size are based on similar statistical tests performed at the subthreshold and spiking level. The MDF was determined as the distance between the positions that elicited a significant increase of the spike discharge (one-tailed t test, $P < 0.01$) when compared with the shuffled discharge elicited for a similar duration period. The visually evoked subthreshold response strength was measured by the integral of the depolarizing component of the stimulus-locked waveform over a 300-ms period starting at the stimulus onset, and compared with that obtained from similar durations of shuffled activity (t test, $P < 0.01$). A linear analysis, relating response strength with the eccentricity from the MDF center, was restricted to the regions where significant responses were evoked, and did not take into account "silent" regions. For each cell, the spatial sensitivity hill profile was fitted by the best pair of lines (least-mean-square criteria), whose intersection with the threshold level of significant response defined the outer diameter of the depolarizing subthreshold field.
13. C. Blakemore and E. A. Tobin, *Exp. Brain Res.* **15**, 439 (1972); B. Gulyas *et al.*, *J. Neurophysiol.* **57**, 1767 (1987).
14. A. M. Sillito *et al.*, *Nature* **378**, 492 (1995).
15. Because visual cortical cells were generally more depolarized at rest (resting potential $V_r = -65.8 \pm 8.7$ mV) than the equilibrium potential for chloride {−77 ± 3.9 mV in vitro [B. W. Connors *et al.*, *J. Physiol.* **406**, 443 (1988)] and −75 mV in vivo [D. E. Shulz *et al.*, *Soc. Neurosci. Abstr.* **19**, 638 (1993)]}, events of positive and negative polarity, when occurring in isolation, may be equated, respectively, with dominating excitatory and inhibitory postsynaptic events. This first-order approximation does not take into account nonlinear interaction between excitation and inhibition [L. J. Borg-Graham *et al.*, *Nature* **393**, 369 (1998)]. Furthermore, assuming a reversal potential close to 0 mV for excitatory conductances, detection of glutamate-mediated events is largely favored with respect to GABA (γ-aminobutyric acid)-mediated ones. H-fields are therefore underestimated in our study. The qualitative subthreshold D-field extents reported by Pei *et al.* (9) are difficult to compare with our own results because of a limited sample size. In addition, their recordings were performed at more depolarized membrane potentials (−30 or −50 mV), where inhibitory hyperpolarizing responses may mask partially the D-field responses, and response amplitudes were measured at a fixed latency.
16. J. P. Jones and L. A. Palmer, *J. Neurophysiol.* **58**, 1187 (1987).
17. Reverse correlation analysis: A d.c. offset was applied to the high-pass filtered voltage records (1 Hz, elliptic filter) such as to center the mode of the membrane potential distribution on a null value. Successive local extrema were defined as being separated by at least 0.5-mV amplitude. Depolarizing events were selected as local positive maxima. Hyperpolarizing events were defined as local minima whose amplitude remained below −1 mV. To assess the statistical significance of the maps, we carried out similar procedures of correlation counts (established over a 25-ms window) in the reverse and forward directions. The reverse-correlation delay [varied from −200 to 0 (retrograde) and 0 to 200 ms (forward) with a 1-ms step] was optimized independently for each visual field pixel such as to maximize the z score given by [number of counts (reverse) − mean (forward)]/SD (forward). The forward procedure allowed us to empirically establish the distribution of the maximal count obtained in a given pixel, under the null hypothesis of independent output and input processes, and define a one-tailed rejection threshold (statistical significance of 1%). The maps presented here are thus without any temporal significance and focus on the spatial structure of the receptive field. Measures of the spatial extent of maps independent of their patchiness were expressed by the diameter of the disk covering the same total area, expressed in degrees of visual angle.

18. Response latencies were given by the time of the first significant deviation of the derivative of the low-pass filtered (5-ms wide gaussian) averaged membrane potential waveform (t test, $P < 0.005$). The measure was validated when the peak of the rising waveform was significantly higher than that measured during the prestimulus trigger condition (t test, $P < 0.01$). Latency profiles were significantly (least-mean-square optimization) fitted by two straight lines (average $<r>^2 = 0.77$ with 2D impulse-like input and 0.88 with long bars), the intersection of which defined the retinal position of the latency basin center (Fig. 4, B and C). This center was superimposed on or close to the MDF center (relative eccentricity: 0.85 ± 0.7°).
19. Despite the fact that both the latency and the strength of the response were highly correlated with the relative eccentricity from the MDF center, both features of the postsynaptic response were weakly correlated together, thus reinforcing the hypothesis that the causative independent variable is the relative eccentricity itself.
20. Z. F. Kisvarday and U. T. Eysel, *Eur. J. Neurosci.* **5**, 1558 (1993).
21. A similar range of ASHP values is found in the adult cat if one takes into account the dependency of the cortical magnification factor on retinal eccentricity [K. Albus, *Exp. Brain Res.* **24**, 181 (1975); R. J. Tusa *et al.*, *J. Comp. Neurol.* **177**, 213 (1978)]. Furthermore, the ASHP values derived from individual latency basins are not significantly linked to the absolute retinal eccentricity of the discharge field of the recorded cells.
22. A. Grinvald *et al.*, *J. Neurosci.* **14**, 2545 (1994).
23. F. Chavane, V. Bringuier, Y. Frégnac, data not shown.
24. The typical speed of action potential propagation along horizontal excitatory connections is 0.15 to 0.60 m/s in T. Murakoshi *et al.* [*Neurosci. Lett.* **163**, 211 (1993)], 0.16 m/s in D. A. Nelson and L. C. Katz [*Neuron* **15**, 23 (1995)], and 0.35 m/s in J. A. Hirsch and C. D. Gilbert [*J. Neurosci.* **11**, 1800 (1991)]. A similar estimate is found for inhibitory connections: 0.06 to 0.20 m/s in P. Salin and D. A. Prince [*J. Neurophysiol.* **75**, 1589 (1996)].
25. The divergence of the terminal field of thalamocortical fibers extends over a 1- to 2-mm radius on average in the plane of cortical layers [A. L. Humphrey *et al.*, *J. Comp. Neurol.* **233**, 159 (1985)]. This value, replotted in visual field coordinates, is on the order of 1° to 2° of visual angle for central representation of the visual field and remains too low to explain the size of the D-field, which was found to be 4 to 15 times as large. Furthermore, the conduction velocity of X and Y thalamocortical axons is 10 to 100 times as fast as that derived from our measurements; the average ASHP value derived from our recordings is on the order of 0.15 m/s, whereas the conduction velocities of X and Y thalamic axons are, respectively, on the order of 8 and 20 m/s in H. P. Hoffmann and J. Stone [*Brain Res.* **32**, 460 (1971)].
26. A. C. Rosenquist, *Cereb. Cortex* **3**, 81 (1985).
27. Using identical stimuli, we obtained LGN ($n = 6$) and optic radiation ($n = 3$) discharge fields of restricted size (1.3° ± 0.6°). These controls preclude possible lateral excitation by light scatter in the retina.
28. A. Das and C. D. Gilbert, *Nature* **375**, 780 (1995).
29. We thank P. Godement, K. Grant, and P.-M. Lledo for helpful comments. We are indebted to L. Borg-Graham and C. Monier for patch electrode data, to D. E. Shulz and V. Ego for LGN recordings, and to P. Baudot, who participated in some of the experiments. This work was supported by CNRS, PROGRES-INSERM, AFIRST, GIS-Cognisciences, and Human Frontier Science Program (RG0103/1998-B) grants to Y.F.

28 July 1998; accepted 21 December 1998

Chemical Etiology of Nucleic Acid Structure: Comparing Pentopyranosyl-(2′→4′) Oligonucleotides with RNA

M. Beier, F. Reck, T. Wagner, R. Krishnamurthy, A. Eschenmoser*

All four members of the family of pentopyranosyl-(2′→4′) oligonucleotide systems that contain β-ribo-, β-xylo-, α-lyxo-, or α-arabinopyranosyl units as repeating sugar building blocks are found to be much stronger Watson-Crick base-pairing systems than RNA. The α-arabinopyranosyl system is the strongest of all and in fact belongs to the strongest oligonucleotide base-pairing systems known. Whatever the chemical determinants by which nature selected RNA as a genetic system, maximization of base-pairing strengths within the domain of pentose-derived oligonucleotide systems was not the critical selection criterion.

A chemical understanding of the criteria by which nature chose ribo- and deoxyribonucleic acids as genetic systems would constitute a central element of any theory of the origin of the particular kind of chemical life that we know today. The quest for such an understanding may be taken up by experiment by systematically synthesizing potential alternatives to the natural nucleic acids and comparing them with RNA with respect to those chemical properties that are fundamental to RNA's biological function (*1*). For such an alternative to be selected for study, we require it to be structurally derivable from a $(CH_2O)_n$ aldosugar ($n = 6$, 5, or 4) by the same type of potentially natural chemistry that allows the structure of RNA to be derived from ribose (*2*). This strategy is an attempt to mimic a hypothetical natural process that may have led to the selection of RNA: a process of combinatorial molecular assembly and functional selection within the domain of sugar-based oligonucleotides. In principle, such an experimental etiological analysis of nucleic acid structure is unbiased with respect to the question of whether RNA first came into being abiotically or biotically.

Our previous studies involving the β-hexopyranosyl-(4′→6′) oligonucleotide family had shown that base pairing in allo-, altro-, and glucopyranosyl oligonucleotides is uniformly much weaker than in RNA (*3*). Comparison with the properties of the 2′-deoxy, 3′-deoxy, and 2′,3′-dideoxyallopyranosyl analogs (*4*) demonstrated that the weaker base pairing is due to intrastrand steric hindrance in the pairing conformation ("too many atoms") (*3*). These findings led us to refocus our studies on the less bulky pentopyranosyl series, where it was discovered that the β-ribopyranosyl-(2′→4′) oligonucleotide system, the pyranosyl isomer of RNA (p-RNA), exhibits Watson-Crick pairing that is far stronger than that in RNA (*5*). Here we show that the same is true for the entire family of pentopyranosyl-(2′→4′) oligonucleotide systems that have the nucleotide base in the equatorial position of the pyranose chair (Scheme 1).

Scheme 2 summarizes the syntheses of the phosphoramidite building blocks **4**, **9**, and **13**, each prepared from the corresponding nucleosides containing adenine or thymine as the nucleobase (*6*, *7*). The preparation of oligomers in the lyxo- and xylopyranosyl series followed the (2′→4′) strategy previously applied in the p-RNA series (*5*). Inversely, oligomer synthesis in the α-arabinopyranosyl series was chosen to proceed in the (4′→2′) direction because the axial 4′-hydroxyl is the least reactive to electrophilic derivatization among the three hydroxyl groups (*8*).

Table 1 summarizes T_m values (the temperature at which about 50% of duplex molecules are dissociated into single strands) and thermodynamic data for five different octamer duplexes of each of the four pentopyranosyl-(2′→4′) oligonucleotide systems, determined in buffered 0.15 M sodium chloride solution at pH 7.0 (see also Fig. 1). Duplex formation was further characterized by temperature-dependent circular dichroism (CD) spectroscopy (Fig. 2) as well as by confirmation of strand stochiometry by determination of ultraviolet (UV) mixing curves

The Skaggs Institute for Chemical Biology at The Scripps Research Institute, 10550 North Torrey Pines Road, La Jolla, CA 92037, USA, and Laboratorium für Organische Chemie, Eidgenössische Technische Hochschule (ETH), Universitätstrasse 16, CH-8092 Zürich, Switzerland.

*To whom correspondence should be addressed.